Journal of Optics

TOPICAL REVIEW

A review of polarization-based imaging technologies for clinical and preclinical applications

IOP Publishing Journal of Optics
J. Opt. **22** (2020) 123001 (18pp) https://doi.org/10.1088/2040-8986/abbf8a

Topical Review

A review of polarization-based imaging technologies for clinical and preclinical applications

Jessica C Ramella-Roman[1,2], Ilyas Saytashev[1,2] and Mattia Piccini[1,3]

[1] Department of Biomedical Engineering, College of Engineering and Computing, Florida International University, Miami, FL 33174, United States of America
[2] Department of Ophthalmology, Herbert Wertheim College of Medicine, Florida International University, Miami, FL 33199, United States of America
[3] Department of Information Engineering, University of Modena and Reggio Emilia, Via Pietro Vivarelli 10-41125, Modena, Italy

E-mail: jramella@fiu.edu

Received 8 May 2020, revised 10 August 2020
Accepted for publication 1 October 2020
Published 11 November 2020

Abstract
Polarization-based imaging can provide new diagnostic capabilities in clinical and preclinical studies. Various methodologies of increasing complexity have been proposed by different groups in the last 30 years. In this review we focus on the most widely used methods in polarization imaging including co- and cross-polarized-based imaging, Mueller matrix imaging, and polarization sensitive optical coherence tomography, among others. This short primer in optical instrumentation for polarization-based imagery is aimed at readers interested in including polarization in their imaging processes.

Keywords: polarization, scattering, birefringence, polarization sensitive optical coherence tomography, Mueller matrix, stokes vectors

(Some figures may appear in colour only in the online journal)

1. Introduction

The use of polarized light illumination and filtering for biomedical applications has a long history. Polarized light is sensitive to structural component and materials with elevated birefringence hence it has been used extensively to investigate the extracellular matrix of several biological environments, including the skin [1–3], the eye cornea [4], connective tissue, and many more.

There are three recognized mechanisms that influence the status of the polarization of light as it travels through a biological media: depolarization, retardation, and diatten uation.

Depolarization occurs primarily due to multiple scattering of light, and incoherent addition of the scattered electromagnetic fields. In biological media scattering is generally very high, caused by a variety of components (organelles, nuclei, collagen fibrils bundles, cell membrane to name a few). Different polarization states—linear, circular or elliptical—depolarize at different rates as will be illustrated later in this review.

Linear retardation is the phase shift between two orthogonal linear polarization states (0° and 90° or +45° and −45°, for example). Circular retardation, also called optical rotation, is the difference in phase between right circular and left circular polarized light travelled in a medium. Both linear and circular retardation components contribute to a total retardation of a media. Typically, fibrous structures such as the skin, the cornea, the sclera, tendon, cardiac tissue, and many others, strongly exhibit retardation.

Diattenuation, also called dichroism, is generally considered the smallest of all the effects in biological media and arises from polarization-selective attenuation of the electrical field.

This review paper focuses on imaging applications of polarimetry in biology and medicine. Clearly, the technological and scientific development of these imaging modalities spur from previous work in atmospheric physics, chemistry, and microscopy [5–12]. We will limit the review to the imaging of bulk tissue, *in vivo* and *ex vivo*, where the effect of multiply-scattering photons cannot be ignored.

2. Polarized light

2.1. Fundamentals

In its classic formulation light transfer can be characterized utilizing the concept of electromagnetic fields propagating as waves through media. The spatio-temporal field is a vector where the electric field $\boldsymbol{E}(\boldsymbol{r},t)$ and magnetic field $\boldsymbol{H}(\boldsymbol{r},t)$ are coupled. Polarization is a property of electromagnetic radiation that relates to the position ($\boldsymbol{r}$) in time (t) of the electric field $\boldsymbol{E}$**.** The state of the electromagnetic wave $\boldsymbol{E}$ can be represented by two independent field components, $\boldsymbol{E_x}(\boldsymbol{r},t)$ and $\mathbf{E}_y(\boldsymbol{r},t)$, orthogonal to each other and lying in the plane perpendicular to the direction of propagation. If we consider the z direction of our reference frame for simplicity, we can represent mathematically the propagating electromagnetic field with two transverse components,

$$\begin{aligned} \mathrm{E}_x(z,t) &= \mathrm{E}_{0x}\cos(\omega t - kz + \delta_x) \\ \mathrm{E}_y(z,t) &= \mathrm{E}_{0y}\cos(\omega t - kz + \delta_y) \end{aligned} \tag{1}$$

where E_{0x} and E_{0y} are the maximum amplitude, δ_x and δ_y are phases, for the two directions x and y, and the term ωt-kz is the propagator, where k is the wave number, and ω is angular frequency. The vectors $\boldsymbol{E_x}$ and $\boldsymbol{E_y}$ arise as the field propagates.

In order to simplify the calculations for polarized light transfer through optical media and optical components, two different formalisms are commonly used, the Stokes–Mueller calculus and the Jones calculus.

2.2. Stokes–Mueller calculus

The Stokes formalism, described by George G Stokes in 1852, shows that any state of polarization of light can be expressed with four measurable quantities, arranged into a vector form. The Stokes vector is composed of four real measurable quantities (S_0,S_1,S_2,S_3 or I,Q,U,V) that relate directly to the polarization ellipse and the optical field [13].

$$\begin{bmatrix} S_0 \\ S_1 \\ S_2 \\ S_3 \end{bmatrix} = \begin{bmatrix} I \\ Q \\ U \\ V \end{bmatrix} = \begin{bmatrix} E_{0x}^2 + E_{0y}^2 \\ E_{0x}^2 - E_{0y}^2 \\ 2E_{0x}E_{0y}\cos(\delta) \\ 2E_{0x}E_{0y}sin(\delta) \end{bmatrix}. \tag{2}$$

$S_0^2 \geqslant S_1^2 + S_2^2 + S_3^2$ where the equal sign is used for completely polarized light and the > sign is for unpolarized or partially polarized light.

The orientation angle of the polarization ellipse can then be calculated through the Stokes vector as $\eta = \frac{1}{2}\tan^{-1}\left(\frac{S_2}{S_1}\right)$ and ellipticity is $\psi = \frac{1}{2}\sin^{-1}\left(\frac{S_3}{S_0}\right)$.

A parameter often used in image polarimetry is the degree of polarization P

$P = \frac{\left(S_1^2+S_2^2+S_3^2\right)^{1/2}}{S_0}$, $P = 1$ for completely polarized light and $P = 0$ for complete depolarization.

While the Stokes parameter can then be used to characterize the status of the polarization of light, another framework is necessary to characterize the media and optical elements interacting with a light beam. The Mueller calculus, introduced by Mueller [14], can be used to describe the changes in amplitude, direction, and relative phase (via S_3) of the orthogonal field components E_x and E_y.

Given an input Stokes vector S and a Mueller matrix M characterizing the media, an output Stokes vector can be calculated as

$$S_{OUT} = MS_{IN}M = \begin{bmatrix} m_{11} & m_{12} & m_{13} & m_{14} \\ m_{21} & m_{22} & m_{23} & m_{24} \\ m_{31} & m_{32} & m_{33} & m_{34} \\ m_{41} & m_{42} & m_{43} & m_{44} \end{bmatrix}. \tag{3}$$

Multiple optical elements can be combined with this formalism to calculate the output Stokes vector, knowing its input state.

$$S_{out} = M_n \ldots . \bullet M_4 \bullet M_3 \bullet M_2 \bullet M_1 \bullet S_{input}. \tag{4}$$

Stokes vectors and Mueller matrices operate incoherent superimpositions of light, hence although unable to describe interference or diffraction, are capable of dealing with field depolarization.

2.3. Jones calculus

When coherence is of interest the Jones calculus must be utilized. Introduced in 1941 [15–19], the Jones vector operates on amplitudes and not intensities like the Stokes vectors. The Jones vector in fact takes the form of equation (5):

$$\vec{E} = \begin{pmatrix} E_x \\ E_y \end{pmatrix}. \tag{5}$$

An electric vector E^{input} traveling through an optical element or scattered by a particle is transformed into E^{out} according to equation (6)

$$\begin{pmatrix} E_x^{out} \\ E_y^{out} \end{pmatrix} = J \begin{pmatrix} E_x^{input} \\ E_y^{input} \end{pmatrix} \tag{6}$$

where the Jones matrix $J = \begin{pmatrix} j_{11} & j_{12} \\ j_{21} & j_{22} \end{pmatrix}$ is composed of four, often complex, elements j.

Similar to Mueller matrices, the matrix product of multiple Jones matrices can be used to characterize a light beam travelling through multiple optical elements of known

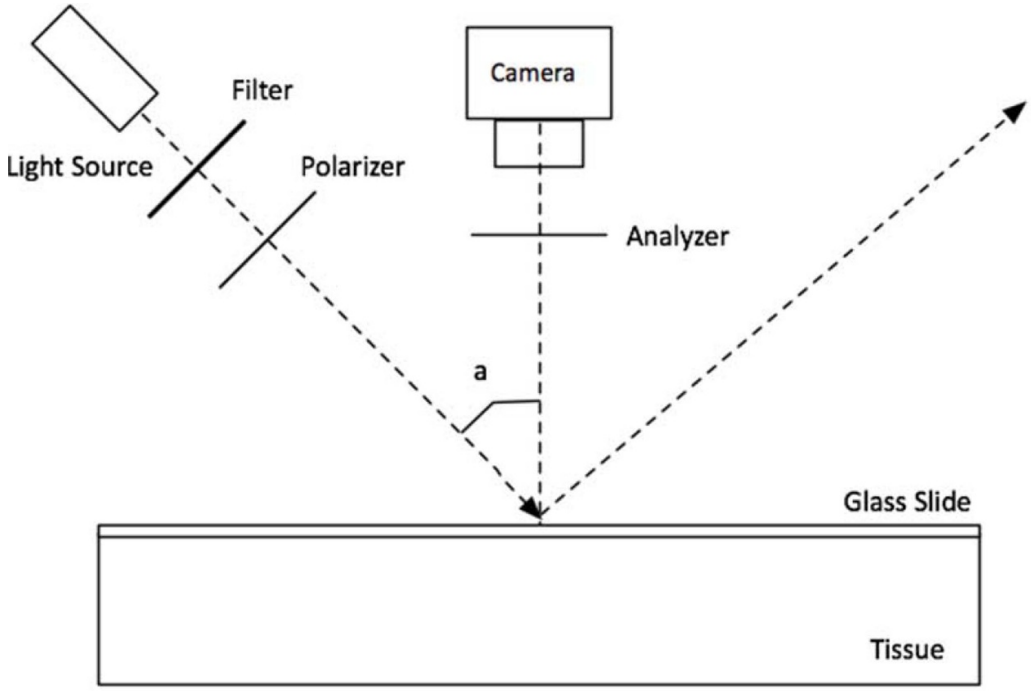

Figure 1. Typical imaging system based linear polarization gating.

Jones matrices. Unlike Stokes–Mueller calculus, Jones calculus describes only fully polarized light-matter interactions, therefore it is not directly applicable to describing partial or full depolarization.

3. Incoherent systems

3.1. Linearly polarized imaging systems

Early work in biomedical applications of polarized light imaging focused on gating of linearly polarized light for glare minimization, image quality improvement, superficial or deep surface imaging. An early report on the use of polarized sunglasses as well as cross-polarization imagery in dermatology is attributed to Anderson in 1991 [20]. Images of rosacea in cross-polarization demonstrated how the technique could be used to enhance vascular contrast and minimize the glare from the rough skin surface. In 2000, Jacques *et al* [21] proposed the mathematical manipulation of co- and crossed-polarized light imaging to enhance surface contrast. The main elements of their systems are shown in figure 1. An incoherent light source, such as a light emitting diode, a xenon lamp, or a flash, was filtered with a narrow band filter. Light was polarized with a linear polarizer, and impinged on a sample at an angle *a*. A digital camera was positioned normal to the sample such that it could avoid most of the glare created by the air–tissue interface. Finally, an analyzer on a rotational stage was positioned in front of the camera to filter the back-reflected polarized light. A glass slide was placed on the sample with a gel or water matching layer to minimize the rough surface polarized back-scatter from the surface. Morgan *et al* later showed that the glass interface could be removed [22] by adding circular polarized light sensing as well as using rotating orthogonal polarization [23].

In later work, Jacques *et al* [2] used the layout of figure 1 to enhance the contrast of skin cancer and other lesions margins. In their work two images were acquired: one where the source and detector polarizer's optical axes were co-aligned (co-polarized detection, *Ipar*), and one where the analyzer's optical axis was perpendicular to the source polarizer's optical axis (cross-polarized detection, *Iper*).

The resulting image contrast (*Pol*), or the degree of linear polarization, was calculated as

$$Pol = \frac{Ipar - Iper}{Ipar + Iper} = \frac{\sqrt{Q^2 + U^2}}{I}. \tag{7}$$

The *Pol* images have several advantages, as they eliminate superficial pigmentation (as found in freckles) and enhance surface contrast. It is thought that the disruption of the dermal collagen in dermal-invasive forms of skin cancer provides a contrast mechanism for discriminating healthy and cancerous skin.

Demos *et al* [24, 25] explored the spectral dependence of polarized light penetration in biological media with an apparatus similar to the one shown in figure 1. Cross-polarization images at wavelength ranges between 600 nm and 970 nm were acquired, and spectral polarization difference imaging was utilized to demonstrate subsurface imaging at long depths.

Groner *et al* [26] recognized early on that cross-polarization could be used to enhance superficial vascular contrast in intravital microscopy, and applied this imaging technique in

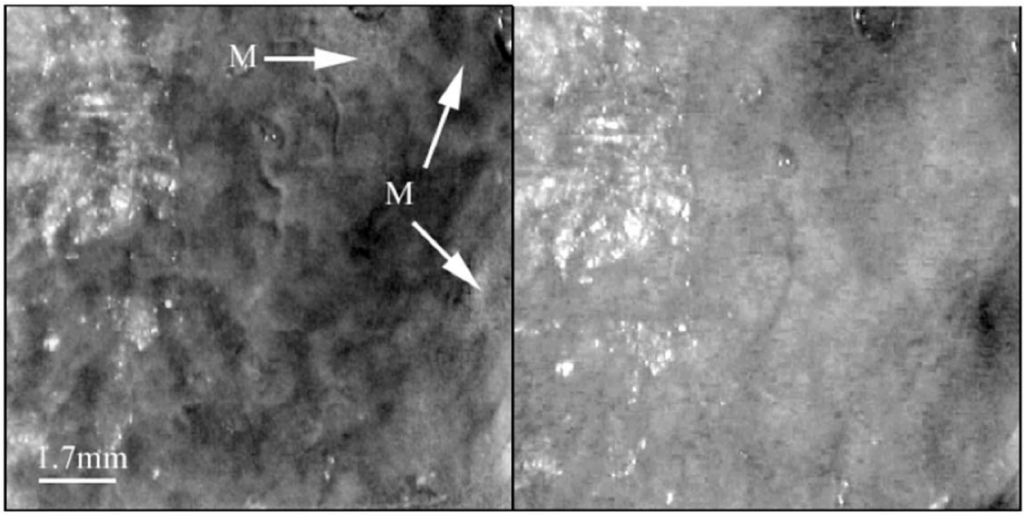

Figure 2. Melanoma image obtained with a portable snapshot system based on a polarizing beamsplitter. Images are from 'Design, testing and clinical studies of a handheld polarized camera'. Reproduced with permission from [34].

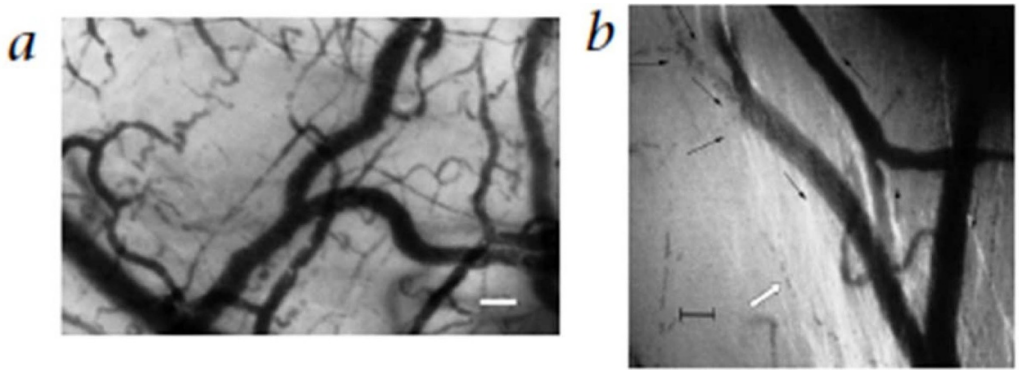

Figure 3. OPS images of human microcirculation. Reproduced with permission from [26]. (a) Sublingual microcirculation. (b) Pial microcirculation bar length is ~100 μm.

studies of brain perfusion, pancreatic and hepatic microcirculation, and many other clinical applications [26–31]. Although their system was based on co-axial illumination and detection the principle is very similar to what is shown in figure 1. Linear polarizers were used for both illumination and detection and the wavelength used was 540 nm to utilize the increased absorption of hemoglobin.

Several groups have used linear polarization as a way to enhance surface roughness contrast for biomedical imaging. Anderson had shown that co-polarized [20] illumination was particularly sensitive to surface architecture. Bargo *et al* also used a goniometric polarized system to study skin wrinkles [32, 33].

A number of snapshot systems based on multichannel acquisition using polarized beam splitter cubes [26, 34] have also been devised to facilitate and accelerate the acquisition of polarization-sensitive images. Figure 2 shows the results obtained with a prototype handheld polarized light camera, which produce images of a sample combining two linearly polarized reflected images. A similar principle has been adopted by Groner *et al* to study microcirculation noninvasively (figure 3).

3.2. Elliptically polarized imaging systems

Several authors have studied the impact of particle size, density, and index of refraction on light polarization [35]. This work, started by the atmospheric optics community has been translated into biophotonics, where scattering due to nuclei, organelles, and other submicron tissue constructs limit light penetration and backscattered polarization [36]. Early work showed that circular polarization was maintained for larger depth compared to linearly polarized light [37]. Computational work based on Monte Carlo simulations confirmed this finding, and showed that the mean visitation depth for linearly polarized light was about two mean free paths (MFPs), while for circularly polarized light it was about 10 MFP [38]. Elliptically polarized light with various degrees of ellipticity was in between 2 and 10 MFP, opening the door to polarization-based optical tomography. Recently, Sridhar *et al* [39] proposed a new protocol of polarization gating that focuses on elliptically-polarized light. This approach allows for the elimination of multiply scattered photons improving contrast and penetration depth, so that deep subsurface features can be reconstructed with higher accuracy [38, 39].

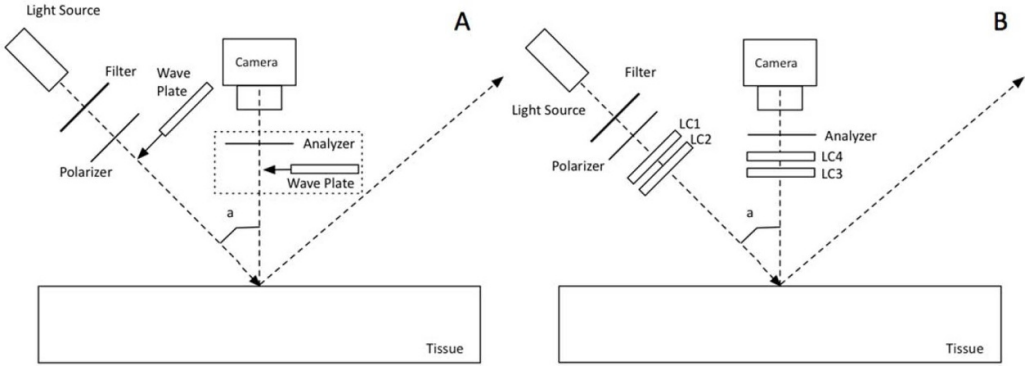

Figure 4. (A) Mueller matrix polarimeter, a quarter wave plate, is inserted in the layout when circular illumination and sensing are desired. (B) LCVR-based Mueller matrix polarimeter.

Instruments have been devised to calculate either partial or the full Stokes vector, and Mueller matrix. Partial systems include the rotating polarizer ellipsometers [40, 41] and combination of spatial frequency domain imaging and rotating polarizer [42]. They are suitable in calculation of the degree of linear polarization as well as the orientation of anisotropic tissues, by providing the direction of fast optical axis [43] in these structures.

3.3. Stokes vector polarimeters

Complete imaging systems relying the transmitted or reflected Stokes vector through bulk tissue require an extension of the instrumentation shown in figure 1. As shown in equation (2), the Stokes vector contains information on the polarization state of a beam, including its ellipticity. Hence, optical retarders or wave plates are usually introduced in the system to generate or measure elliptical or circular states. In order to calculate the Stokes vector parameters four intensities need to be measured, corresponding to different positions of the polarized optical elements in the detection arm. In figure 4(a), a typical Stokes vector polarimeter is highlighted (dashed box). It consists of a wave plate with retardance ϕ at a fixed position with respect to the main reference frame and a polarizer on a rotational stage (can be rotated by an angle θ). The resulting measured intensity $I(\theta,\phi)$ is a function of these elements' position, and the incident beam's status of polarization expressed by the Stokes vector $S = [S_0, S_1, S_2, S_3]$.

$$I(\theta,\phi) = \frac{1}{2}\left(S_0 + S_1 cos\left(2\theta\right) + S_2 sin\left(2\theta\right) cos\left(\phi\right) - S_3 sin\left(2\theta\right) sin\left(\phi\right)\right). \quad (8)$$

From equation (8), four measurements of $I(\theta,\phi)$ with known θ and ϕ result in a system of linear equations, from which the Stokes vector can be calculated as

$$\begin{bmatrix} S_0 \\ S_1 \\ S_2 \\ S_3 \end{bmatrix}_{out} = \begin{bmatrix} I(0^0,0^0) + I(90^0,0^0) \\ I(0^0,0^0) - I(90^0,0^0) \\ 2I(45^0,0^0) - S_0 \\ S_0 - 2I(45^0,90^0) \end{bmatrix} = \begin{bmatrix} I(0^0,NP) + I(90^0,NP) \\ I(0^0,NP) - I(90^0,NP) \\ 2I(45^0,NP) - S_0 \\ S_0 - 2I(45^0,90^0) \end{bmatrix}. \quad (9)$$

In practice [44], the measurement of S_0, S_1, S_2 is conducted by removing the quarter waveplate in front of the polarizer (NP = not in place, figure 4(a)). Only the last term, S_3, requires this element in order to measure an elliptical/circular state. Many other methods to calculate the Stokes vector of a beam have been devised, including ones that did not require the removal of the waveplate but maintained constant relative position between waveplate and polarizer to acquire S_0, S_1, S_2. The drawback of this approach is that two optical elements require rotation instead of one [45], the advantage being that the wave plate impact on the beam is always considered. Other methods include the rotation of the ¼ wave retarder followed by the linear polarizer at a fixed angle θ and Fourier analysis of the transmitted beam [13], or the use of liquid crystal variable retarders (LCVRs, figure 4(b)).

A snapshot imaging Stokes vector system can also be approached with beamsplitter cubes, Savart plates, Wollaston prisms, and other methods. A good review of the various methodologies is offered by Tyo *et al* [46]. Design of systems based on use of beamsplitter cubes (figure 5) is straightforward and easy to follow with captured images on the detection cameras representing as orthogonal as possible polarization states. Unfortunately, their implementation is rather difficult due to the precision one must maintain in aligning all the components, which requires either precision stages or high precision machining.

Furthermore, up to four different cameras are necessary for this approach. Recently Savart-plates-based polarimeters have been proposed, primarily for nonmedical applications [47, 48]. These are interferometric systems that require only one camera, the polarization information is embedded in the system spatial carrier fringes (figure 6).

Unfortunately, the Savart plates must be designed depending of the need of the system, of a specific thickness, furthermore these polarimeters work at narrow optical bandwidth

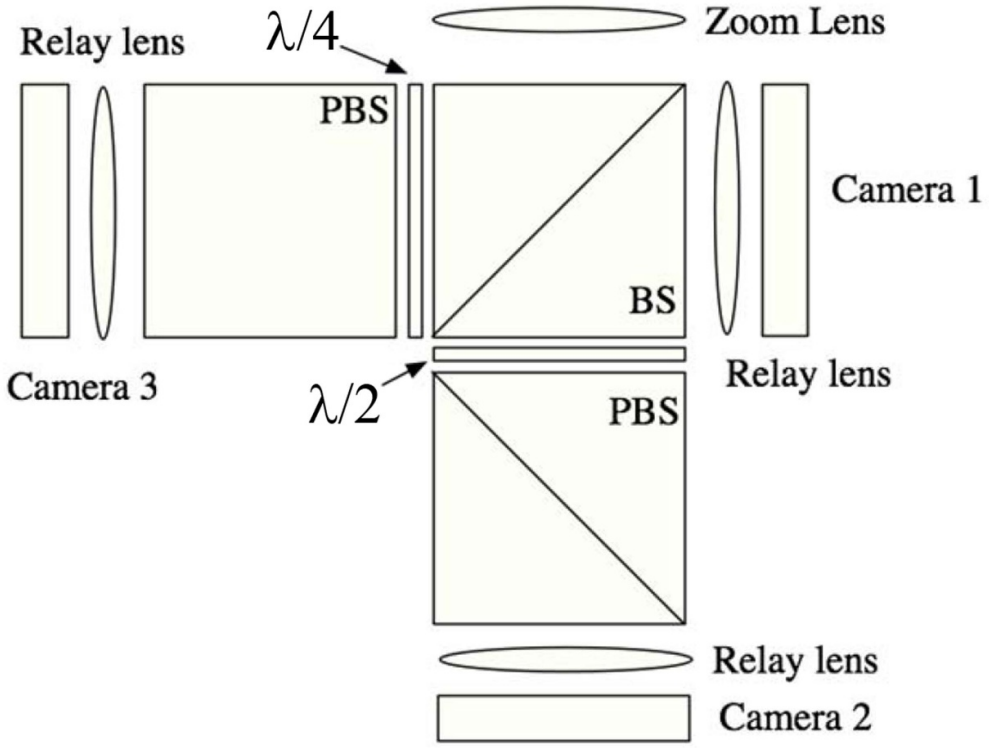

Figure 5. Snapshot Stokes vector polarimeter. Reproduced with permission from [46]. The fourth camera is out of the plane of the page after the quarter-wave retarder.

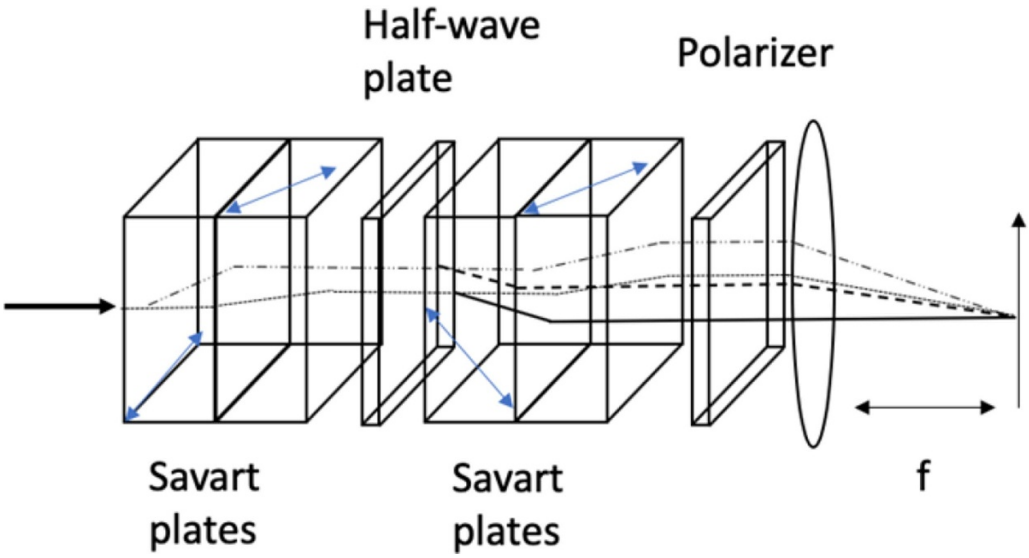

Figure 6. Snapshot Stokes vector polarimeter. Reproduced with permission from [49].

[50] although some investigators have been able to push this limit up to 50 nm [51].

DeHoog *et al* [52] developed a Stokes vector snapshot fundus ophthalmoscope, based on Savart plates. This approach is particularly suitable for environments prone to motion artifacts (figure 7).

Gonzalez *et al* [49] used a portable system based on two sets of Savart plates to develop a portable system to image the cervix. They deployed the system in rural India imaging patients seeking early signs of cervical dysplasia.

3.4. Mueller matrix polarimeters (MMPs)

The scheme for measuring the Mueller matrix includes two polarimetric parts, the first one that generates the polarization states before the specimen (polarization state generator (PSG)) and a second one that analyses the result of the interaction (polarization state analyzer (PSA)). There are several possible configurations that allow us to collect all the polarization states necessary to compose the matrix. In figure 4 we show some possible combination of PSG and PSA to achieve

a Mueller matrix [53, 54]. A straightforward [13] implementation includes setting the light source at three linear states (polarizer set at 0° (subscript H), 45° (subscript P), 90° (subscript V), no waveplate in place) and one right circular state (polarizer at 45°, ¼ waveplate at 0° subscript R) [55, 56]. And the detection of the Stokes vector of each source (four elements per vector × 4 measurements = 16 values), I Q U V are again the element of the Stokes vector. So I_H is the first element of the Stokes vector obtained with a linearly polarized source at 0° (H).

$$M = \begin{bmatrix} \frac{1}{2}(I_H + I_V) & \frac{1}{2}(I_H - I_V) & I_P - M(1,1) & I_R - M(1,1) \\ \frac{1}{2}(Q_H + Q_V) & \frac{1}{2}(Q_H - Q_V) & Q_P - M(2,1) & Q_R - M(2,1) \\ \frac{1}{2}(U_H + U_V) & \frac{1}{2}(U_H - U_V) & U_P - M(3,1) & U_R - M(3,1) \\ \frac{1}{2}(V_H + V_V) & \frac{1}{2}(V_H - V_V) & V_P - M(4,1) & V_R - M(4,1) \end{bmatrix}. \tag{10}$$

Stokes vector and Mueller matrix systems based on variable retarder constructed of birefringent nematic liquid crystals (ferroelectric liquid crystal [57, 58] (FLC) and liquid crystal variable retarders (LCVR)) are common in imaging (figure 4(b)), they do not require moving elements and are computer controllable. Ghassemi *et al* [59] utilized the LCVR approach in an out-of-plane Stokes vector system to quantify surface roughness and apply it to the assessment of melanoma. Roughness was quantified through the principal angle of polarization η obtained by measuring the back-reflected Stokes vector. Pierangelo *et al* and Agarwal *et al* utilized both partial and full Mueller matrix LCVR polarimeters to diagnose both colon and cervical cancer [60–65].

Dual rotating mueller matrix polarimeters are also very common [66–69]. These systems utilize two retarders (generally quarter wave plates) and fixed polarizer, with a layout similar to figure 4(a) where the waveplate is left in place rather than being removed. The wave plates are rotated at an angular frequency of ω and N ω, respectively (where $N = 5$ is common). The modulated signal obtained through the rotation of the waveplate is analyzed with Fourier transforms, the Mueller matrix elements are then retrieved from the Fourier coefficients.

Photoelastic modulator (PEM)-based Stokes [70] vector and Mueller matrix [71, 72] polarimeters have also been proposed. These systems have high acquisition rates and can be utilized in both scanning and camera-based imaging systems. The clinical use of the system may be limited by instrumentation needed for PEM synchronization and their encumbrance. Arteaga *et al* introduced a four-PEMs based Mueller matrix polarimeter, where modulation of the input and output polarization is achieved through the photoelastic elements [73].

Snapshot Mueller matrix polarimeters, as presented by Dubreuil *et al* [74] and Hagen *et al* [75] distribute the different polarization parameters on several carriers over the spectrum. To do so they utilized birefringent plates with different thicknesses which are wavelength dependent. A typical scheme utilizes two wave plates with thickness e for the state generator, and two with thickness $5e$ in the state analyzer. With this approach, Dubreuil *et al* were able to retrieve the complete Mueller matrix in around 1 ms with a relatively small absolute error on each Mueller matrix element. It is to be noted that the need of achromatic samples for these systems limits their use in biological environments.

3.4.1. MMP calibration methods. While typical lens, mirrors and other nonpolarizing optical elements do not exhibit strong polarization effects, they may contribute to the total error between estimated and actual values of the Stokes vectors delivered to the sample plane and measured after interaction with a sample.

The eigenvalue calibration method (ECM) [76, 77] aims to ensure accuracy of the acquired sample Mueller matrices, doing so by computing both the polarization state generator and analyzer from the measurements performed on reference samples. This method, originally developed by Compain *et al* [77], is based on control theory, applied to a linear system depicted in figure 8.

Any experimentally measured intensity matrix ($\boldsymbol{B}$) is defined by the product between the Mueller matrix of the sample ($\boldsymbol{M}$), the PSG ($\boldsymbol{W}$) and PSA ($\boldsymbol{A}$), (both unknown), which yields to the mathematical model in equation (11). For ECM, a blank set of measurements (no sample) hereafter denoted as $\boldsymbol{B_0}$, and three measurements of well-modeled samples (polarizer at two orientation angles and a waveplate) measurements are required in order to retrieve calibrated PSG and PSA.

$$\mathrm{B} = \mathrm{A}\ \mathrm{M}\ \mathrm{W},\ \mathrm{B}_0 = \mathrm{A}\ \mathrm{W}. \tag{11}$$

The essential steps of ECM are as follows. A second set of matrices $\boldsymbol{C_i}$ for each measurement $\boldsymbol{B_i}$ is constructed, independent from $\boldsymbol{A}$, as shown in equation 12. $\boldsymbol{C_i}$ and $\boldsymbol{M_i}$ are similar by construction, and thus have the same eigenvalues—two real (λ_{R1}, λ_{R2}) and two complex (λ_{C1}, λ_{C2}).

$$\mathrm{C_i} = {\mathrm{B_0}}^{-1}\mathrm{B_i} = \mathrm{W}^{-1}\mathrm{M_i}\mathrm{W} \text{ or } \mathrm{M_i}\mathrm{W} - -\mathrm{W}\ \mathrm{C_i} = 0. \tag{12}$$

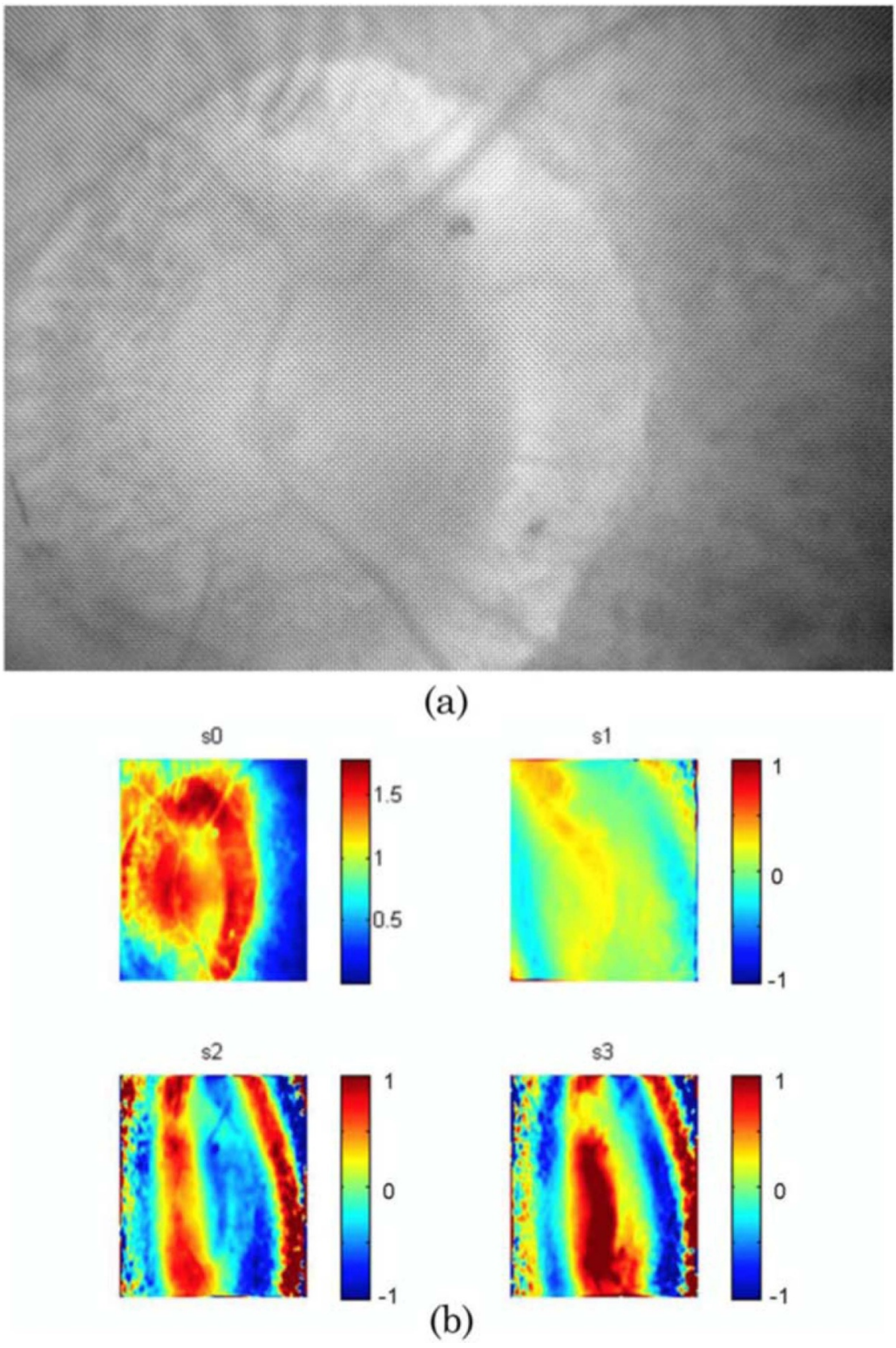

Figure 7. (a) Retina with advanced glaucoma and (b) associated Stokes vector images. Reproduced with permission from [52].

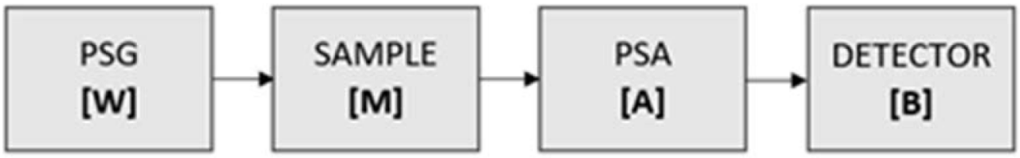

Figure 8. Block diagram representation of a Mueller matrix polarimeter.

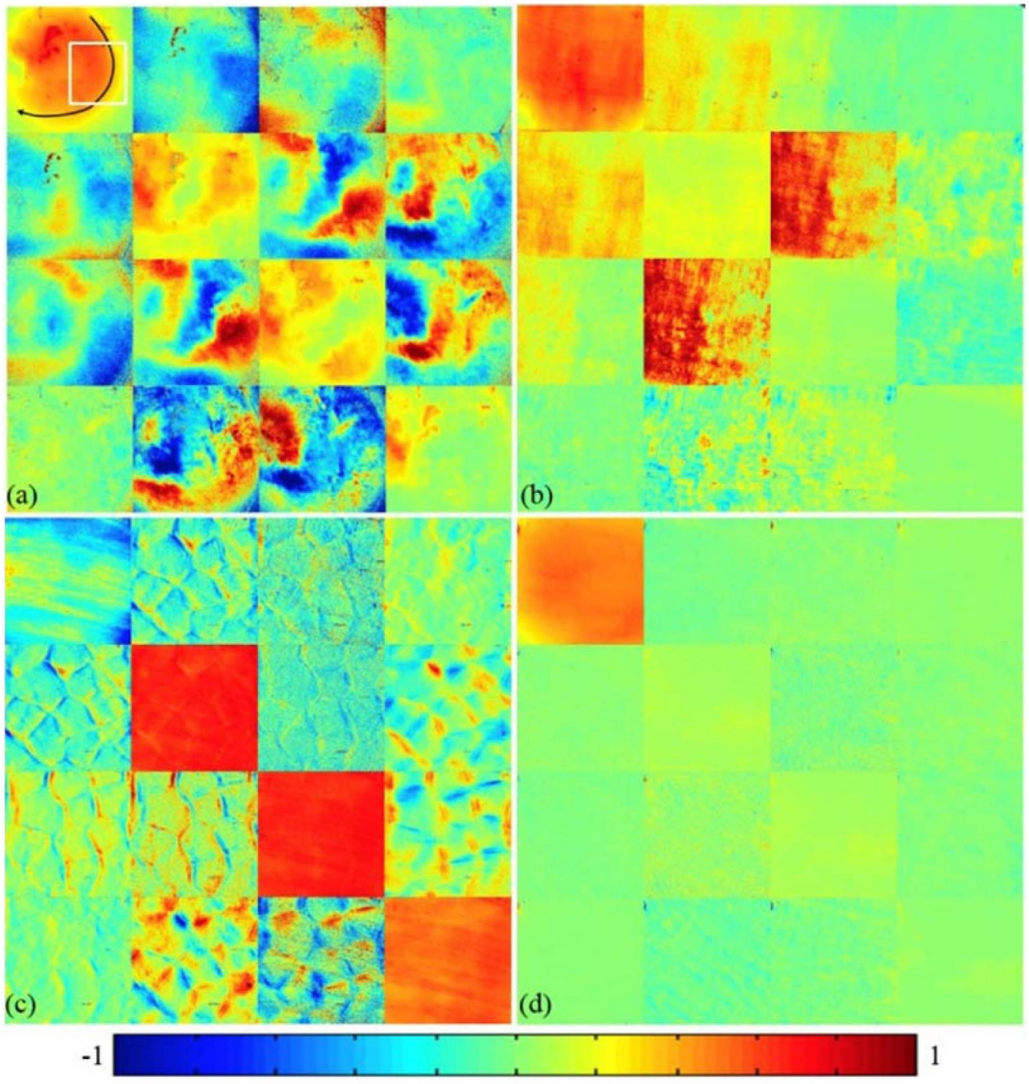

Figure 9. Reproduced with permission from [97]. Experimental results of backscattering Mueller matrices of biological samples: (a) chicken heart tissue (the black arrow line in m11 indicates the approximate orientation of muscle fibers. The white square indicates the approximate area chosen for the calculation of average values of Mueller matrix elements), (b) bovine skeletal muscle tissue, (c) porcine liver tissue, (d) porcine fat tissue.

The Mueller matrix of a high-quality polarizer or waveplate [7], used as reference, take the form of

$$M = \tau \begin{bmatrix} 1 & -\cos 2\psi & 0 & 0 \\ -\cos 2\psi & 1 & 0 & 0 \\ 0 & 0 & \sin 2\psi \cos \Delta & \sin 2\psi \sin \Delta \\ 0 & 0 & \sin 2\psi \sin \Delta & \sin 2\psi \cos \Delta \end{bmatrix} \tag{13}$$

where τ, ψ and Δ are associated to the transmittance, polarizing and phase-shift effect respectively; and relates to a sample's Mueller matrix $\boldsymbol{M}$ through a rotation of optical axis by angle θ, and therefore yields the same eigenvalues:

$$\mathrm{M_i}(\theta, \tau, \psi, \Delta) = \mathrm{Rot}(\theta_\mathrm{i})\ \mathrm{M_i Rot}(-\theta_\mathrm{i}). \tag{14}$$

Hence, by obtaining the intensity matrix $\boldsymbol{B_i}$ and calculating eigenvalues of constructed matrix $\boldsymbol{C_i}$, it is possible to retrieve

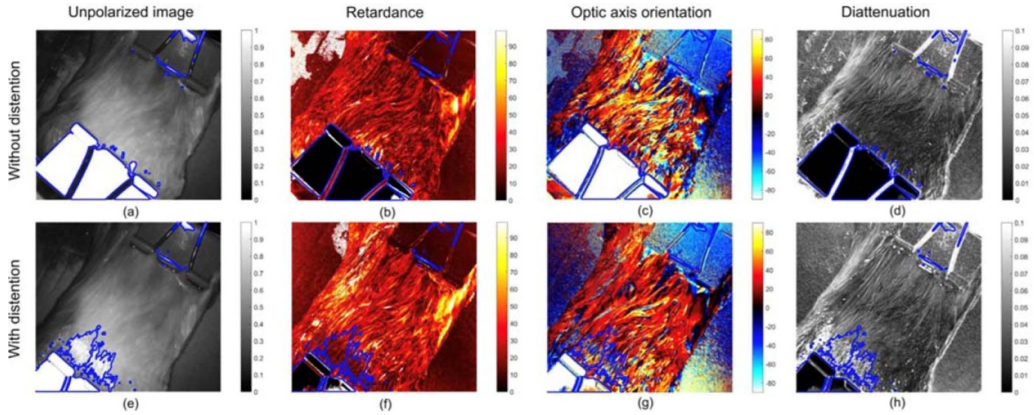

Figure 10. Example of use of decomposition. Reproduced from [79]. CC BY 4.0. The images from the first to the fourth column are respectively unpolarized image, retardance image, optic axis orientation map, diattenuation images of the bladder. Each image shows an area of about 7.8 × 7.8 cm^2. (a)–(d) Images obtained when the bladder was not under distention and (e), (f) are those obtained when the bladder was under distention. Regions enclosed by the blue lines were invalid due to pixel saturation in at least one of the raw images for Mueller polarimetric image reconstruction.

diattenuator-retarder parameters such as transmission, retardation, and diattenuation **independent** of the optical axis rotation:

$$T = \frac{\lambda_{R1} + \lambda_{R2}}{2}, \psi = \tan^{-1}\sqrt{\frac{\lambda_{R1}}{\lambda_{R2}}}, \Delta = \log\sqrt{\frac{\lambda_{c2}}{\lambda_{c1}}} \tag{15}$$

which leads to a concrete representation of a diattenuator-retarder matrix $\boldsymbol{M_i}$ for each calibration measurement. Therefore, equation (12) yields to a system of equations with unknown PSG matrix $\boldsymbol{W}$ and optical axis angle rotational θ_{i} of each optical element:

$$\begin{array}{lll} \mathrm{M_1}(\theta_1)\,\mathrm{W} & -- & \mathrm{W\,C_1} = 0 \\ \mathrm{M_2}(\theta_2)\,\mathrm{W} & -- & \mathrm{W\,C_2} = 0 \\ & \ldots & \\ \mathrm{M_i}(\theta_{\mathrm{i}})\,\mathrm{W} & -- & \mathrm{W\,C_i} = 0. \end{array} \tag{16}$$

This system can be solved for $\boldsymbol{W}$ with a least square regression with an initial guess of optical axis angles θ_{i}. In order to do so, a linear operator $\boldsymbol{K}$ is obtained from the mapping construct $H(X) = MX—XC$, defined from the set of the real matrices $M(R)$ into itself. By definition, the only eigenvector of K associated with a null eigenvalue will be W, leading to the solution

$$\mathrm{KW_{16X1}} = 0 \tag{17}$$

where $K = H^{\mathrm{T}}\,H$. The mathematical approach does not consider the physical limitations [77] of a real system, meaning that the equality $H(W) = 0$ will not be verified in at the actual setup. $0 \approx \lambda_1 << \lambda_2 < \lambda_3 \ldots < \lambda_{16}$

Nonetheless, the eigenvalues of K follow

$$0 \approx \lambda_1 << \lambda_2 << \lambda_3 \ldots < \lambda_{16}.$$

Eventually, the solution W_{16X1} is the eigenvector associated with the smallest eigenvalue. Precise values of optical axis orientation θ_{i} of calibration samples is found through a iterative minimization algorithm by slightly varying θ_{i} values and calculating eigenvalues of $\boldsymbol{K}$. A minimal value of the lowest eigenvalue ensures that we found both precise optical axis orientations and the solution for retrieving the PSG matrix. It is worth noting that the demonstrated method of obtaining matrix W can be implemented for A by using a construct $C_i = B_i\,{B_0}^{-1}$ in equation (11). However, solving equation (10) for $A = B_0\,{W}^{-1}$ is computationally cost-effective.

In some cases, the dispersion in the retardance of optical components can affect the performance of the polarimeter, in this scenario a 4 × 4 Mueller matrix is not enough to ensure an accurate measurement. Good results have been obtained combining eigenvalue calibration with overdetermined polarimetry in the assessment of cornea structure [78].

Another calibration method requires the construction of a data matrix (W) by utilizing a rotating polarizer and a fixed achromatic waveplate. The polarizer is first positioned before the waveplate and then after it, by rotating the polarizer a series of linear and elliptical states are measured spanning the entire Poincaré sphere. This approach requires that both training polarizer and waveplates be well characterized and that their positions are known [79, 80] but the exact position of the polarimeter elements (retarders and polarizers) or their specific retardation is not necessary to achieve successful calibration.

Optimization of the calibration can be done by measuring known Mueller matrices, such as the Mueller matrix of air whose ideal form is shown in equation (18) below. This approach is useful to determine systematic errors in the calibration [81, 82].

$$M_{\mathrm{air}} = \begin{bmatrix} 1 & 0 & 0 & 0 \\ 0 & 1 & 0 & 0 \\ 0 & 0 & 1 & 0 \\ 0 & 0 & 0 & 1 \end{bmatrix}. \tag{18}$$

The condition number of the data matrix is also used to determine the optimal calibration [83]. The condition number

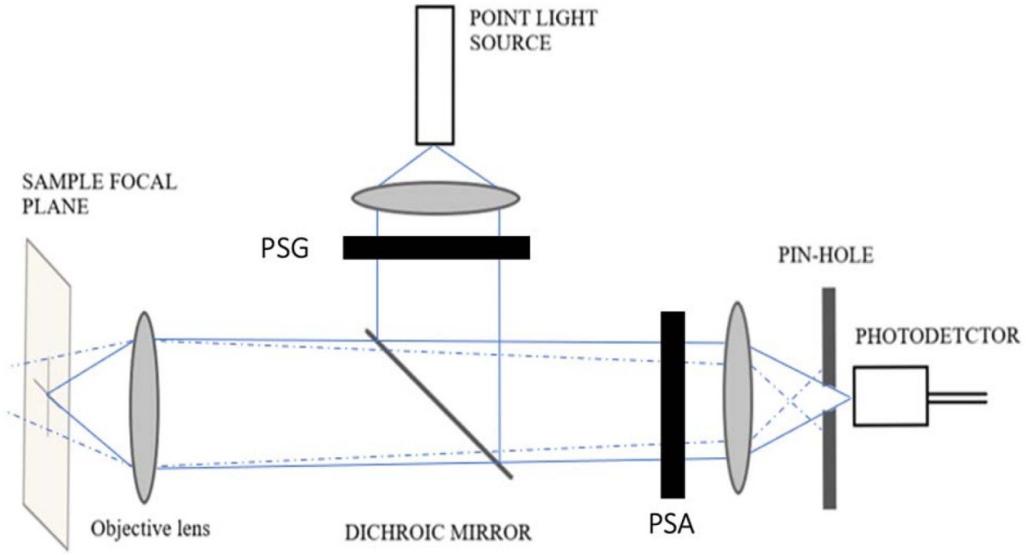

Figure 11. Schematic representation of the effect of a pinhole in confocal microscopy. Black boxes represent PSA and PSG additions necessary for Mueller matrix confocal microscopy.

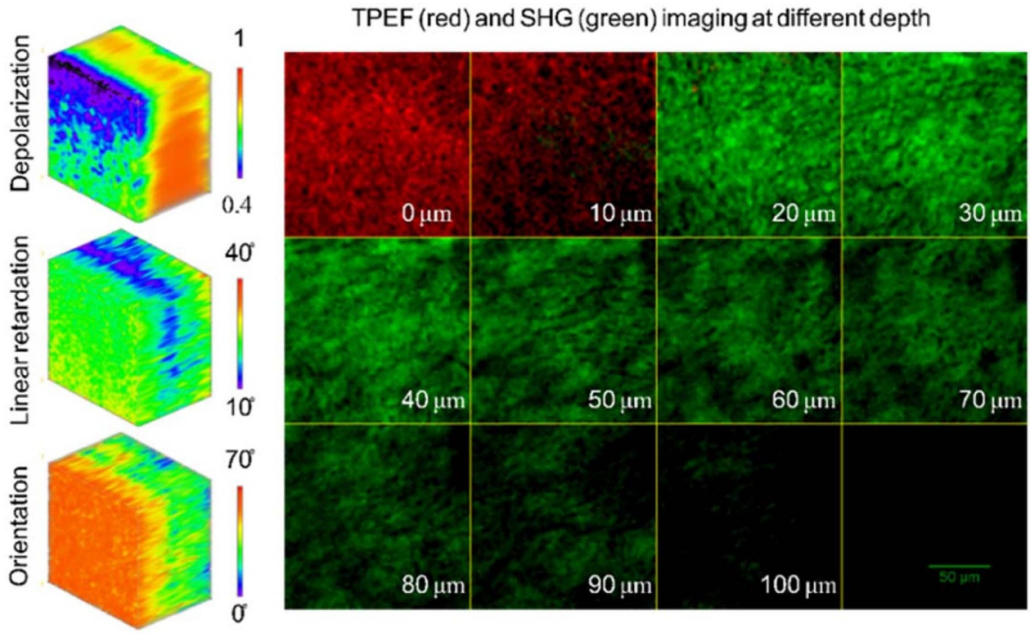

Figure 12. Full-depth two-photon and Mueller matrix confocal imaging of an unstained rat cornea. Reproduced with permission from [78]. 120×120 μm^2 imaging area was taken at the center of a cornea.

is a property of a matrix that determines how near it is to singularity. The smaller the condition number the more independent are matrix rows and columns. Tyo *et al* demonstrated that the theoretical minimum condition number for the data matrix W is $\sqrt{3}$.

Early work utilizing Mueller matrices focused on particle size determination, particle shape [84], as well as subtle changes in the media index of refraction [55, 85–89], and separating cancerous versus precancerous cells [86]. Other investigators studied the influence of the Mueller matrix of anisotropic tissue [90–92] such as muscle, and collagenous structures [93, 94]. Others explored its use in dermatologic applications [95, 96]. Some examples of biological media Mueller matrices measured by Sun *et al* [97] are shown in figure 9.

Following the seminal paper by Lu and Chipman [98] in 1996 many groups have explored Mueller matrix decomposition as a way to isolate different light tissue interaction mechanisms. Mueller matrix decomposition is often used to extract constituent polarization properties from a Mueller matrix of any unknown complex system. Although different types of decomposition have been suggested by some investigators [99], the Lu–Chipman [98] approach remains the most popular in biophotonics yielding three canonical

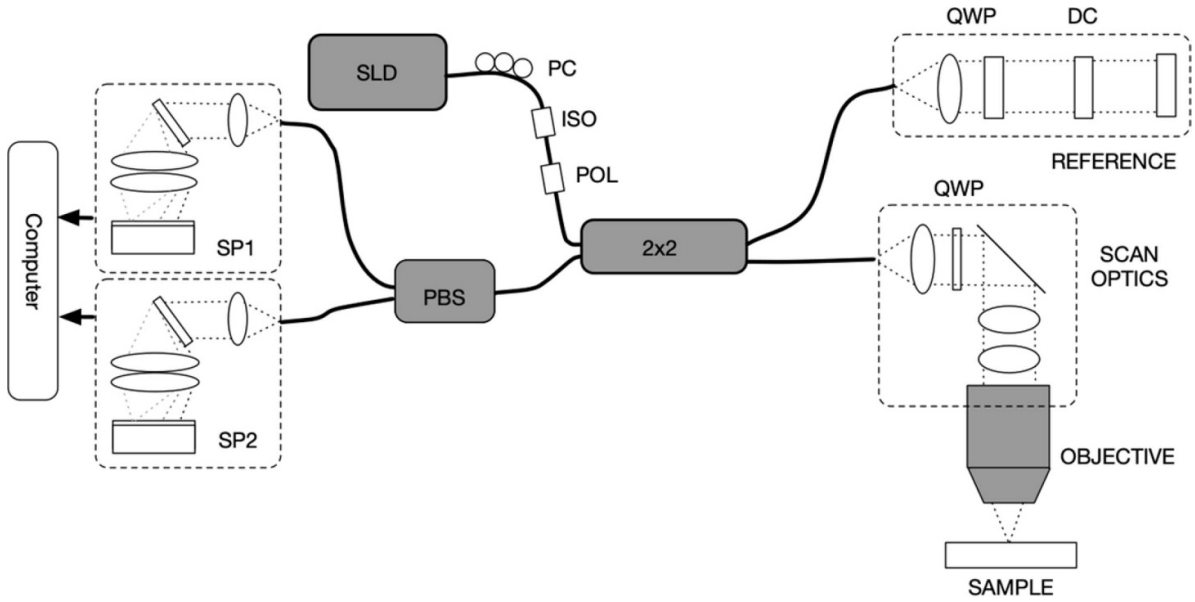

Figure 13. Schematic representation of a spectral domain PS-OCT system. Reproduced from [122]. CC BY 3.0. The system utilizes a polarization-maintaining (PM) fiber-based Michelson interferometer (2 × 2). In the sample arm the beam is stirred to the sample with a pair of galvanometer mirrors. The source consists of a superluminescent diode (SLD). The detectors are two fast spectrometers (SP1 and SP2). A polarizing beam splitter (PBS) redirects the light from the sample arm and reference arm to the spectrometers in two orthogonal polarization states. ISO is an optical isolator and POL a polarizer. QWP elements are quarter wave plates. DC is a dispersion compensation element. PC, polarization controllers.

matrices $M = M_{\Delta} M_{\mathrm{R}} M_{\mathrm{D}}$. A diattenuator matrix M_{D} includes the effects of linear and circular diattenuation, M_{Δ}, accounting for the depolarizing effects of the material, a retarder matrix M_{R} for the effects of the material linear birefringence and optical activity, and a depolarizer matrix. By decomposing the Mueller matrix, we are hence able to isolate mechanisms such as scattering, absorption, retardation, birefringence and so on. Furthermore, the resulting matrices can be analyzed to yield quantitative medium properties that have a demonstrated [100] useful diagnostic power. These parameters are **depolarization, linear retardance** δ (birefringence), **optical rotation** $\boldsymbol{R}$, and **slow axis orientation** θ (the direction of polarization with the larger optical index) and **diattenuation** $\boldsymbol{D}$. Depolarization is caused by multiple scattering and is prominent in biological tissue. In figure 10 [79], we show some examples of this decomposition approach on anisotropic and collagen rich tissue. Retardance and optical axis orientation are parameters of interest in anisotropic material (collagen for biological samples). The propensity of a tissue to have a dominant direction as expressed in some materials can be expressed as alignment index, a value between 0 (no alignment) and 1 (perfect).

Mueller matrix decomposition has been used by to stage cervical cancer in the epithelium by the late Pierangelo *et al* and Rehbinder *et al* [101, 102], as well as determination of early stages of colon cancer [61, 62, 64, 65, 103]. This work focused in large part on establishing contrast mechanisms for these invasive forms of cancer utilizing deviation from uniform retardation values in collagen rich stromal tissue, and has recently shown the capability of distinguishing CIN 3 stage cervical cancer based on these principles *ex vivo* [102]. Shukla *et al* developed a Mueller matrix system for separating normal and dysplastic states in cervical tissue [104]. Chue-Sang *et al* proposed the use of a combined Mueller matrix and polarization sensitive optical coherence tomography system to image highly birefringent tissue, including cervical tissue; the combination of modalities may be used to elucidate local retardation versus cumulative, depolarization depth for polarized light and other parameters [105].

Alali *et al* used Mueller matrix polarimetry for multiple applications including the assessment of local structural disorders of the bladder wall [106] and studies of infarcted myocardium [107]. Together with Gosh *et al* [56, 87, 108–111], this group has also contributed to a better understanding of the fundamental physics of Mueller matrix polarimetry in biological environments as well as the development of tissue mimicking phantoms [56, 110].

3.4.2. Confocal mueller matrix. A confocal microscope acquires sharp images of a sample, removing the blurred effect associated to photons backscattered from out-of-focus positions. This technology is broadly used to resolve the detailed structure of a thick specimen. The idea behind confocal microscopy is to acquire only the signal coming from the focal plane of the objective, while the out-of-focus light is rejected by means of a pinhole. In doing so, each image will represent a specific layer of the whole bulk structure.

Figure 11 depicts the basic operation of a confocal microscope with added PSA and PSG. Here the backscattered light goes through a dichroic mirror that removes the excitation wavelengths. Subsequently, a pinhole selects the light coming from the focal position, that is then acquired by the sensor.

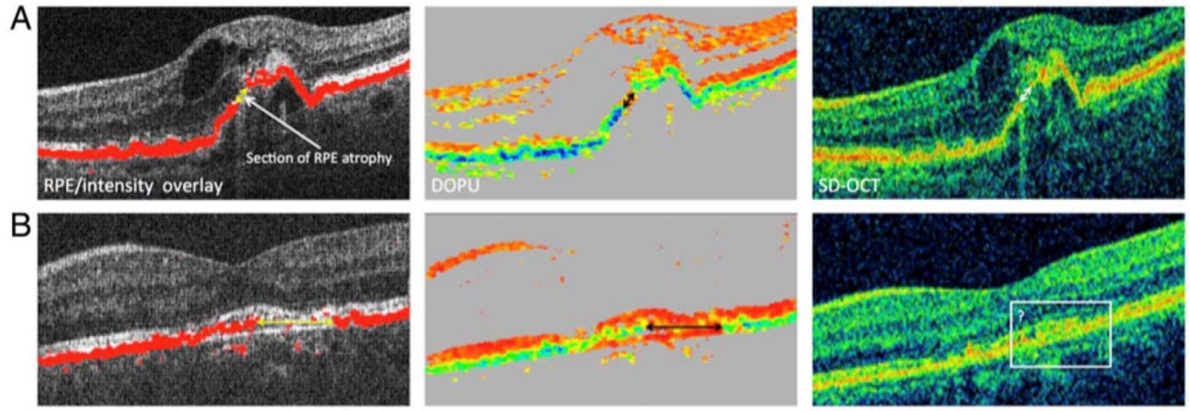

Figure 14. Reproduced from [133]. CC BY 4.0. Comparison of RPE atrophy detection by PS-OCT and intensity-based SD-OCT in eyes with neovascular age-related macular degeneration. (A) The unambiguous identification of RPE atrophy in PS-OCT clearly corresponding to the intensity-based OCT images; (B) illustrates an example where the unambiguous identification of atrophic RPE is only possible using PS-OCT imaging. Note that in (B), it is not possible to clearly identify the borders of the atrophic zone (rectangle). RPE atrophy sections indicating RPE atrophy borders (arrows) are illustrated. DOPU, degree of polarization uniformity; PS-OCT, polarization-sensitive optical coherence tomography; RPE, retinal pigment epithelium; SD-OCT, spectral-domain optical coherence tomography.

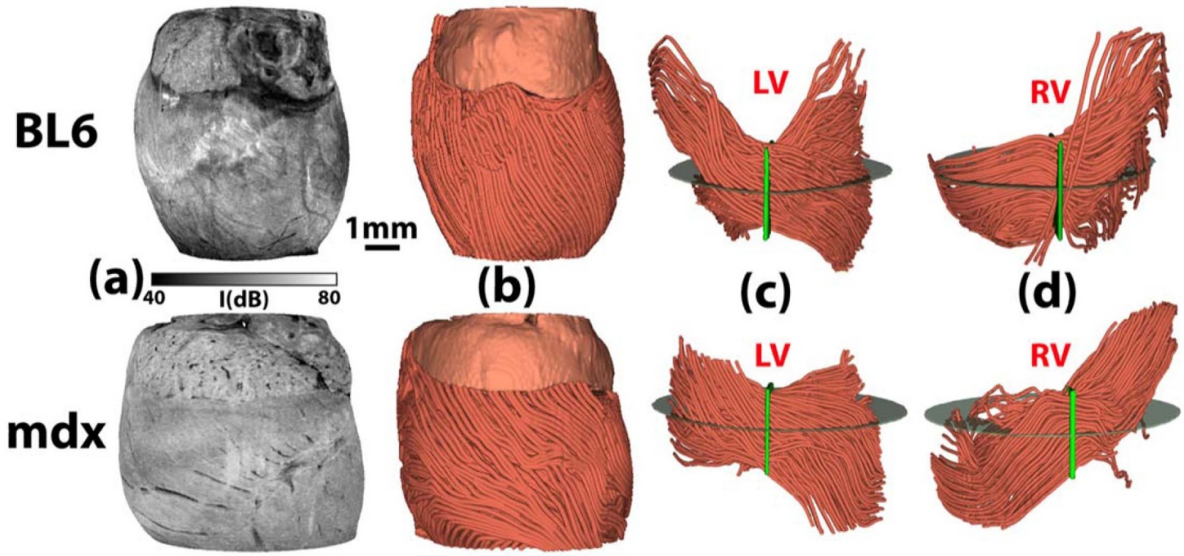

Figure 15. An example of tractotomy based on PS-OCT data from Wang *et al.* (a) Intensity images of a BL6 heart and an mdx heart. (b) The corresponding 3D tractography of the BL6 heart and the mdx heart, both with the left ventricle (LV) facing front. Also shown are depth-resolved tractography showing myofibers passing through a 1.5 mm high region of interest (green plate) across (c) the LV and (d) the right ventricle (RV) of the BL10 and mdx hearts, respectively.

Lara *et al* applied the confocal microscopy approach in order to axially resolve Mueller matrix polarimetry [82]. The idea was further developed by Okoro *et al* for imaging benign and malignant breast tissue using confocal polarimetry with SHG-guided imaging [112, 113]. Saytashev *et al* fully combined nonlinear microscopy imaging with confocal Mueller matrix imaging to investigate the origination of polarimetric signatures (depolarization, retardation) in phantoms and corneal tissues [78]. An example of data obtained with this latter system are shown in figure 12. The depth dependence of the Mueller matrix confocal data can be represented with a volumetric approach, this allows us to separate different regions within a heterogeneous tissue such as the retina. Nonlinear microscopy is used to validate the results.

4. Coherent systems

4.1. Polarization sensitive optical coherence tomography—PS OCT

OCT is a well-established clinical tool, particularly in ophthalmology, as it offers cross sectional images of tissue noninvasively and with a resolution very close to cell size (~5 to 10 μm). PS-OCT is a polarimetric scanning imaging modality [114] and an extension of OCT [115–117]. PS-OCT has been used to

relay information about cross sectional phase-retardation and optical axis orientation and has followed the evolution of OCT in the last two decades.

The time domain system was devised first [118, 119], followed quickly by the spectral domain PS-OCT [120] and then the PS swept source OCT [121]. A typical layout of the spectral domain PS-OCT is shown in figure 13 and was reproduced from Baumann *et al* [122].

With this layout, a full Jones vector can be obtained and then converted into a Stokes vector. Cumulative retardation of a sample can also be obtained with this layout equation (19)

$$\delta = \arctan\left(\frac{I_V}{I_H}\right). \tag{19}$$

Typical images of retardation of collagen rich tissue, such as tendon, exhibit a π periodicity (so-called 'wrapping'). True retardation is generally more desirable, therefore minimization algorithms have been proposed to reconstruct the local retardation from the cumulative [119], as well as approaches based on Monte Carlo algorithms have also been proposed recently [123]. In order to reconstruct a full Mueller matrix using polarization sensitive OCT, multiple input states of polarization [124, 125] are required.

The reader is directed to an excellent review of PS-OCT instrumentation in [114, 126]. Also Lurie *et al* and Ellerbee *et al* [116, 127] showed what arrangement for PS-OCT provides the highest signal to noise ratio. From a polarization standpoint PS-OCT focuses almost uniquely on the retardation property of a media. One promising application is in the determination of collagen retardation and orientation in the cornea [123] as a way to diagnose keratoconus [128] and other degenerative diseases [129, 130]. In the eye, measurements of birefringence and thickness of the retinal nerve fiber layer (RNFL) [131, 132] have also been demonstrated and may be used in the diagnosis of glaucoma. A parameter related to the degree of polarization called the degree of polarization uniformity (DOPU) has also been used in the segment and image the retinal pigmented epithelium (RPE) [133] and is calculated by averaging adjacent pixels of the cross sectional Stokes vector obtained with PS-OCT (figure 14). The RPE has low DOPU values compared to its surroundings, hence DOPU provides and efficient contrast mechanism [134].

Since the PS-OCT relies on the Jones vector, algebra depolarization *per se* is not achievable with these apparatuses, nevertheless the polarization state of the speckles in the images is uncorrelated and it is what provides the departure from the theoretical degree of polarization equal to 1. Another application of PS-OCT is the characterization of scars due to burns [1, 3, 124]. Scars contain highly aligned and packed collagen bundles compared to normal skin that has a mesh like collagen architecture hence the birefringent signature of collagen can be used as a contrast mechanism.

Recently polarized tractotomy, based on PS-OCT, was used to obtain high resolution fiber organization images of cardiac tissues. This modality has been applied to the investigation of heart structural remodeling (figure 15) with results comparable to MRI based diffusion-tensor imaging (DTI) in small animals [135].

4.2. Polarized speckle imaging

Laser speckle imaging is generally used in biophotonics to obtain measurements of perfusion, as the movement of red blood cells within the capillary network decorrelates the speckle to a higher extent than in the nearby tissue. Hence, speckle can be used as a contrast mechanism. Laser speckle imagery is generally conducted in a copolarized arrangement, so to improve the speckle contrast rejecting some of the diffused scattered photons. A novel application of polarized speckle imaging was suggested by Dhadwal *et al* [136] for the diagnosis of skin cancer.

In an extensive clinical study (214 lesions total), she showed that statistical moments of the polarization speckle pattern could be used to differentiate skin lesions. The fourth order moment was used to differentiate melanoma and seborrheic keratosis with very promising sensitivity [136, 137]. This approach relies, in large part, on scattering from the skin lesion rough surface, hence the mechanism is similar to the one proposed by Ghassemi *et al* using incoherent polarized light [59].

5. Conclusions

Polarized light-based imaging is being explored by several groups for its diagnostic power, particularly in instances where tissue is highly anisotropic and birefringent. The retardation caused by such tissue can be used as a contrast mechanism to determine pathological changes in tissue structure [40, 61, 62, 106] and variation in the birefringent element quantity. In particular, polarized light imaging has been used in tissue whose extracellular matrix consists of collagen, a typical example is the skin whose mesh-like collagen structure is disrupted by the onset of skin cancer or by the collagen bulking due to scar formation. Mueller matrix polarimetry and its decomposition is becoming a standard method to isolate this phenomenon, at the same time PS-OCT is making strides with its ability to tomographically resolve birefringent tissue layers. The main limitation of polarized light imagery remains its shallow penetration depth, but some recent studies seem to indicate that the polarization signature can be maintained up to 0.7 mm in depth [38, 39]. Another important limitation for researchers in this field is the lack of standardized optical phantoms that can be used to truly quantify their findings. To our knowledge, the only systematic attempt at constructing phantoms encompassing retardation, depolarization, and attenuation was conducted by Wood *et al* [100] in 2007. This is particularly true for phantoms for PS-OCT where microstructure resolution is critical. Finally, albeit not explored here, computational models for polarized light transfer have been published by several authors, although only a few authors have made them available to the general public [87, 138]. Few of these models include effects of retardation [59] and mostly consider spherical scatters, this is a clear limitation to their use in biological instances where birefringence is at play. Hence future work should be

conducted to ease the limitations described above, and this would greatly advance studies of polarized light imaging in medicine.

Acknowledgments

This work was supported by Herbert Wertheim College of Medicine and the Herbert and Nicole Wertheim Professorship Endowment as well as the STROBE: A National Science Foundation Science & Technology Center under Grant No. DMR 1548924.

ORCID iD

Jessica C Ramella-Roman https://orcid.org/0000-0002-5710-6004

References

[1] Gong P J, Chin L X, Es'haghian S, Liew Y M, Wood F M, Sampson D D and McLaughlin R A 2014 Imaging of skin birefringence for human scar assessment using polarization-sensitive optical coherence tomography aided by vascular masking *J. Biomed. Opt.* **19** 126014
[2] Jacques S L, Ramella-Roman J C and Lee K 2002 Imaging skin pathology with polarized light *J. Biomed. Opt.* **7** 329–40
[3] Sakai S, Yamanari M, Lim Y, Nakagawa N and Yasuno Y 2011 *In vivo* evaluation of human skin anisotropy by polarization-sensitive optical coherence tomography *Biomed. Opt. Express* **2** 2623–31
[4] Westphal P, Kaltenbach J M and Wicker K 2016 Corneal birefringence measured by spectrally resolved Mueller matrix ellipsometry and implications for non-invasive glucose monitoring *Biomed. Opt. Express* **7** 1160–74
[5] Hovenier J W, V. D. Mee C V M and Domke H 2004 Astrophysics and space science library *Transfer of Polarized Light in Planetary Atmospheres: Basic Concepts and Practical Methods* (Dordrecht: Kluwer) p 258
[6] McCrone W C, McCrone L B and Delly J G 1978 *Polarized Light Microscopy* (Ann Arbor, MI: Ann Arbor Science Publishers) p 251
[7] Azzam R M A and Bashara N M 1977 *Ellipsometry and Polarized Light* (North-Holland: Amsterdam) p 529
[8] Brosseau C 1998 *Fundamentals of Polarized Light: A Statistical Optics Approach* (New York: Wiley) p 405
[9] Shurcliff W A 1962 *Polarized Light; Production and Use* (Cambridge, MA: Harvard University Press) p 207
[10] Kliger D S, Lewis J W and Randall C E 1990 *Polarized Light in Optics and Spectroscopy* (New York: Academic) p 304
[11] Shurcliff W A and Ballard S S 1964 *Polarized Light* (Princeton, NJ: Van Nostrand) p 144
[12] Goldstein D H and Collett E 2003 *Polarized Light* 2nd edn Optical engineering (New York: Marcel Dekker) p 653
[13] Edward C 1993 *Polarized Light Fundamentals and Applications* (New York: Marcel Dekker)
[14] Mueller H 1948 The foundation of optics *J. Opt. Soc. Am.* **38** 661
[15] Jones R C 1941 A new calculus for the treatment of optical systems I. Description and discussion of the calculus *J. Opt. Soc. Am.* **31** 488–93
[16] Jones R C 1942 A new calculus for the treatment of optical systems IV *J. Opt. Soc. Am.* **32** 486–93
[17] Jones R C 1947 A new calculus for the treatment of optical systems V. A more general formulation and description of another calculus *J. Opt. Soc. Am.* **37** 107–10
[18] Jones R C 1956 A new calculus for the treatment of optical systems VIII. Electromagnetic theory *J. Opt. Soc. Am.* **46** 126–31
[19] Jones R C 1948 A new calculus for the treatment of optical systems VII. Properties of the N-matrices *J. Opt. Soc. Am.* **38** 671–85
[20] Anderson R R 1991 Polarized light examination and photography of the skin *Arch. Dermatol.* **127** 1000–5
[21] Jacques S L, Roman J R and Lee K 2000 Imaging superficial tissues with polarized light *Lasers Surg. Med.* **26** 119–29
[22] Morgan S P and Stockford I M 2003 Surface-reflection elimination in polarization imaging of superficial tissue *Opt. Lett.* **28** 114–6
[23] Morgan S P, Zhu Q, Stockford I M and Crowe J A 2008 Rotating orthogonal polarization imaging *Opt. Lett.* **33** 1503–5
[24] Demos S G, Radousky H B and Alfano R R 2000 Deep subsurface imaging in tissues using spectral and polarization filtering *Opt. Express* **7** 23–8
[25] Demos S G and Alfano R R 1997 Optical polarization imaging *Appl. Opt.* **36** 150–5
[26] Groner W, Winkelman J W, Harris A G, Ince C, Bouma G J, Messmer K and Nadeau R G 1999 Orthogonal polarization spectral imaging: a new method for study of the microcirculation *Nat. Med.* **5** 1209–12
[27] Genzel-Boroviczeny O, Strotgen J, Harris A G, Messmer K and Christ F 2002 Orthogonal polarization spectral imaging (OPS): a novel method to measure the microcirculation in term and preterm infants transcutaneously *Pediatr. Res.* **51** 386–91
[28] Langer S, Born F, Hatz R, Biberthaler P and Messmer K 2002 Orthogonal polarization spectral imaging versus intravital fluorescent microscopy for microvascular studies in wounds *Ann. Plast. Surg.* **48** 646–53
[29] Langer S, Harris A G, Biberthaler P, von Dobschuetz E and Messmer K 2001 Orthogonal polarization spectral imaging as a tool for the assessment of hepatic microcirculation: a validation study *Transplantation* **71** 1249–56
[30] Uhl E, Lehmberg J, Steiger H J and Messmer K 2003 Intraoperative detection of early microvasospasm in patients with subarachnoid hemorrhage by using orthogonal polarization spectral imaging *Neurosurgery* **52** 1307–15
[31] von Dobschuetz E, Biberthaler P, Mussack T, Langer S, Messmer K and Hoffmann T 2003 Noninvasive in vivo assessment of the pancreatic microcirculation: orthogonal polarization spectral imaging *Pancreas* **26** 139–43
[32] Bargo P R and Kollias N 2006 Measurement of skin texture as a function of age through polarization imaging *J. Invest. Dermatol.* **126** 45
[33] Bargo P R and Kollias N 2010 Measurement of skin texture through polarization imaging *Br. J. Dermatol.* **162** 724–31
[34] Ramella-Roman J C, Lee K, Prahl S A and Jacques S L 2004 Design, testing, and clinical studies of a handheld polarized light camera *J. Biomed. Opt.* **9** 1305–10
[35] Schmitt J M, Gandjbakhche A H and Bonner R F 1993 Use of polarized-light to discriminate short-path photons in a multiply scattering medium *Appl. Opt.* **32** 2186
[36] Hielscher A H, Mourant J R and Bigio I J 1997 Influence of particle size and concentration on the diffuse backscattering of polarized light from tissue phantoms and biological cell suspensions *Appl. Opt.* **36** 125–35
[37] Mackintosh F C, Zhu J X, Pine D J and Weitz D A 1992 Polarization memory of multiply scattered-light - reply *Phys. Rev.* B **45** 8165

[38] Rehn S, Planat-Chretien A, Berger M, Dinten J M, Deumie C and da Silva A 2013 Depth probing of diffuse tissues controlled with elliptically polarized light *J. Biomed. Opt.* **18** 16007

[39] Sridhar S and Da Silva A 2016 Enhanced contrast and depth resolution in polarization imaging using elliptically polarized light *J. Biomed. Opt.* **21** 071107

[40] Garcia-Caurel E, De Martino A, Gaston J P and Yan L 2013 Application of spectroscopic ellipsometry and Mueller ellipsometry to optical characterization *Appl. Spectrosc.* **67** 1–21

[41] Qi J, Ye M, Singh M, Clancy N T and Elson D S 2013 Narrow band 3 × 3 Mueller polarimetric endoscopy *Biomed. Opt. Express* **4** 2433–49

[42] Yang B, Lesicko J, Sharma M, Hill M, Sacks M S and Tunnell J W 2015 Polarized light spatial frequency domain imaging for non-destructive quantification of soft tissue fibrous structures *Biomed. Opt. Express* **6** 1520–33

[43] Swami M K, Manhas S, Buddhiwant P, Ghosh N, Uppal A and Gupta P K 2006 Polar decomposition of 3 × 3 Mueller matrix: a tool for quantitative tissue polarimetry *Opt. Express* **14** 9324–37

[44] Clarke D and Grainger J F 1971 *Polarized Light and Optical Measurement* 1st edn (Oxford: Pergamon) p 187

[45] Berry H G, Gabrielse G and Livingston A E 1977 Measurement of the Stokes parameters of light *Appl. Opt.* **16** 3200–5

[46] Tyo J S, Goldstein D L, Chenault D B and Shaw J A 2006 Review of passive imaging polarimetry for remote sensing applications *Appl. Opt.* **45** 5453–69

[47] Oka K and Saito N 2006 Snapshot complete imaging polarimeter using Savart plates *P. Soc. Photo-Opt. Ins.* **6295** 29508

[48] Luo H, Oka K, DeHoog E, Kudenov M, Schiewgerling J and Dereniak E L 2008 Compact and miniature snapshot imaging polarimeter *Appl. Opt.* **47** 4413–7

[49] Gonzalez Mariacarla M K, Karl K, Vijaya S, Edward D, Purnima M and Jessica C. R-R 2020 Design and implementation of a portable colposcope Mueller matrix polarimeter *J. Biomed. Opt.* submitted

[50] Liu Z, Yang W F, Ye Q H, Hong J, Gong G Y and Zheng X B 1934-1940 Alignment error analysis of the snapshot imaging polarimeter *Appl. Opt.* **55** 2016

[51] Saito N, Odate S, Otaki K, Kubota M, Kitahara R and Oka K 2013 Wide field snapshot imaging polarimeter using modified Savart plates *Proc. SPIE* **8873**

[52] DeHoog E, Luo H, Oka K, Dereniak E and Schwiegerling J 1663-1667 Snapshot polarimeter fundus camera *Appl. Opt.* **48** 2009

[53] Ambirajan A and Look D C 1994 Optimum angles for a Mueller matrix polarimeter *Polarization Anal. Meas.* II **2265** 314–26

[54] Pezzaniti J L and Chipman R A 1990 Imaging polarimeters for optical metrology *Proc. SPIE* **1317** 280–94

[55] Cameron B D, Rakovi M J, Mehrubeo Lu M, Kattawar G W, Rastegar S, Wang L V and Cote G L 1998 Measurement and calculation of the two-dimensional backscattering Mueller matrix of a turbid medium: errata *Opt. Lett.* **23** 1630

[56] Ghosh N, Wood M F and Vitkin I A 2008 Mueller matrix decomposition for extraction of individual polarization parameters from complex turbid media exhibiting multiple scattering, optical activity, and linear birefringence *J. Biomed. Opt.* **13** 044036

[57] Peinado A, Lizana A and Campos J 2013 Optimization and tolerance analysis of a polarimeter with ferroelectric liquid crystals *Appl. Opt.* **52** 5748–57

[58] Baba J S, Chung J R, DeLaughter A H, Cameron B D and Cote G L 2002 Development and calibration of an automated Mueller matrix polarization imaging system *J. Biomed. Opt.* **7** 341–9

[59] Ghassemi P, Lemaillet P, Germer T A, Shupp J W, Venna S S, Boisvert M E, Flanagan K E, Jordan M H and Ramella-Roman J C 2012 Out-of-plane Stokes imaging polarimeter for early skin cancer diagnosis *J. Biomed. Opt.* **17** 076014

[60] Agarwal N, Yoon J, Garcia-Caurel E, Novikova T, Vanel J C, Pierangelo A, Bykov A, Popov A, Meglinski I and Ossikovski R 2015 Spatial evolution of depolarization in homogeneous turbid media within the differential Mueller matrix formalism *Opt. Lett.* **40** 5634–7

[61] Antonelli M R, Pierangelo A, Novikova T, Validire P, Benali A, Gayet B and De Martino A 2010 Mueller matrix imaging of human colon tissue for cancer diagnostics: how Monte Carlo modeling can help in the interpretation of experimental data *Opt. Express* **18** 10200–8

[62] Antonelli M R, Pierangelo A, Novikova T, Validire P, Benali A, Gayet B and De Martino A 2011 Impact of model parameters on Monte Carlo simulations of backscattering Mueller matrix images of colon tissue *Biomed. Opt. Express* **2** 1836-51

[63] Novikova T *et al* 2016 Special section guest editorial: antonello De Martino (1954–2014): in memoriam *J. Biomed. Opt.* **21** 71101

[64] Pierangelo A, Manhas S, Benali A, Fallet C, Antonelli M R, Novikova T, Gayet B, Validire P and De Martino A 2012 Ex vivo photometric and polarimetric multilayer characterization of human healthy colon by multispectral Mueller imaging *J. Biomed. Opt.* **17** 066009

[65] Pierangelo A, Manhas S, Benali A, Fallet C, Totobenazara J L, Antonelli M R, Novikova T, Gayet B, De Martino A and Validire P 2013 Multispectral Mueller polarimetric imaging detecting residual cancer and cancer regression after neoadjuvant treatment for colorectal carcinomas *J. Biomed. Opt.* **18** 046014

[66] Azzam R M 1978 Photopolarimetric measurement of the Mueller matrix by Fourier analysis of a single detected signal *Opt. Lett.* **2** 148

[67] Smith M H 2002 Optimization of a dual-rotating-retarder Mueller matrix polarimeter *Appl. Opt.* **41** 2488–93

[68] Goldstein D H 1992 Mueller matrix dual-rotating retarder polarimeter *Appl. Opt.* **31** 6676–83

[69] Liu S, Chen X and Zhang C 2015 Development of a broadband Mueller matrix ellipsometer as a powerful tool for nanostructure metrology *Thin Solid Films* **584** 176–85

[70] Alali S, Yang T Y and Vitkin I A 2013 Rapid time-gated polarimetric Stokes imaging using photoelastic modulators *Opt. Lett.* **38** 2997–3000

[71] Alali S and Vitkin I A 2013 Optimization of rapid Mueller matrix imaging of turbid media using four photoelastic modulators without mechanically moving parts *Opt. Eng.* **52** 103114

[72] Alali S, Gribble A and Vitkin I A 2016 Rapid wide-field Mueller matrix polarimetry imaging based on four photoelastic modulators with no moving parts *Opt. Lett.* **41** 1038–41

[73] Arteaga O, Freudenthal J, Wang B and Kahr B 2012 Mueller matrix polarimetry with four photoelastic modulators: theory and calibration *Appl. Opt.* **51** 6805–17

[74] Dubreuil M, Rivet S, Le Jeune B and Cariou J 2007 Snapshot Mueller matrix polarimeter by wavelength polarization coding *Opt. Express* **15** 13660–8

[75] Hagen N, Oka K and Dereniak E L 2007 Snapshot Mueller matrix spectropolarimeter *Opt. Lett.* **32** 2100–2

[76] Laude-Boulesteix B, De Martino A, Drevillon B and Schwartz L 2004 Mueller polarimetric imaging system with liquid crystals *Appl. Opt.* **43** 2824–32

[77] Compain E, Poirier S and Drevillon B 1999 General and self-consistent method for the calibration of polarization modulators, polarimeters, and mueller-matrix ellipsometers *Appl. Opt.* **38** 3490–502

[78] Saytashev I, Saha S, Chue-Sang J, Lopez P, Laughrey M and Ramella-Roman J C 2020 Self validating Mueller matrix micro-mesoscope (SAMMM) for the characterization of biological media *Opt. Lett.* **45** 2168–71

[79] Qi J and Elson D S 2016 A high definition Mueller polarimetric endoscope for tissue characterisation *Sci. Rep.* **6** 25953

[80] Boulbry B, Ramella-Roman J C and Germer T A 2007 Improved method for calibrating a Stokes polarimeter *Appl. Opt.* **46** 8533–41

[81] Twietmeyer K M and Chipman R A 2008 Optimization of Mueller matrix polarimeters in the presence of error sources *Opt. Express* **16** 11589–603

[82] Lara D and Dainty C 2005 Double-pass axially resolved confocal Mueller matrix imaging polarimetry *Opt. Lett.* **30** 2879–81

[83] Tyo J S 2002 Design of optimal polarimeters: maximization of signal-to-noise ratio and minimization of systematic error *Appl. Opt.* **41** 619–30

[84] Yang P, Wei H L, Kattawar G W, Hu Y X, Winker D M, Hostetler C A and Baum B A 2003 Sensitivity of the backscattering Mueller matrix to particle shape and thermodynamic phase *Appl. Opt.* **42** 4389–95

[85] Cameron B D, Rakovic M J, Mehrubeoglu M, Kattawar G W, Rastegar S, Wang L V and Cote G L 1998 Measurement and calculation of the two-dimensional backscattering Mueller matrix of a turbid medium *Opt. Lett.* **23** 485–7

[86] Hielscher A H and Bartel S 2000 Diffuse backscattering Mueller matrix analysis for tissue diagnostics with polarized light *Opt. Biopsy Iii* **3917** 43–53

[87] Cote D and Vitkin I 2005 Robust concentration determination of optically active molecules in turbid media with validated three-dimensional polarization sensitive Monte Carlo calculations *Opt. Express* **13** 148–63

[88] Rakovic M J, Kattawar G W, Mehrubeoglu M B, Cameron B D, Wang L V, Rastegar S and Cote G L 1999 Light backscattering polarization patterns from turbid media: theory and experiment *Appl. Opt.* **38** 3399–408

[89] Mehrubeoglu M, Kehtarnavaz N, Rastegar S and Wang L V 1998 Effect of molecular concentrations in tissue-simulating phantoms on images obtained using diffuse reflectance polarimetry *Opt. Express* **3** 286–98

[90] He H, Zeng N, Li W, Yun T, Liao R, He Y and Ma H 2010 Two-dimensional backscattering Mueller matrix of sphere-cylinder scattering medium *Opt. Lett.* **35** 2323–5

[91] Guo Y, Zeng N, He H, Yun T, Du E, Liao R, He Y and Ma H 2013 A study on forward scattering Mueller matrix decomposition in anisotropic medium *Opt. Express* **21** 18361–70

[92] Du E, He H, Zeng N, Guo Y, Liao R, He Y and Ma H 2012 Two-dimensional backscattering Mueller matrix of sphere-cylinder birefringence media *J. Biomed. Opt.* **17** 126016

[93] Li X, Ranasinghesagara J C and Yao G 2008 Polarization-sensitive reflectance imaging in skeletal muscle *Opt. Express* **16** 9927–35

[94] Ramella-Roman J C, Nayak A and Prahl S A 2011 Spectroscopic sensitive polarimeter for biomedical applications *J. Biomed. Opt.* **16** 047001

[95] Smith M H 2001 Interpreting Mueller matrix images of tissues *Proc. SPIE* **4257** 82–9

[96] Smith M H, Burke P, Lompado A, Tanner E and Hillman L W 2000 Mueller matrix imaging polarimetry in dermatology *Proc. SPIE* **3911** 210–6

[97] Sun M, He H, Zeng N, Du E, Guo Y, Liu S, Wu J, He Y and Ma H 2014 Characterizing the microstructures of biological tissues using Mueller matrix and transformed polarization parameters *Biomed. Opt. Express* **5** 4223–34

[98] Lu S Y and Chipman R A 1996 Interpretation of Mueller matrices based on polar decomposition *J. Opt. Soc. Am. A* **13** 1106–13

[99] Ossikovski R, De Martino A and Guyot S 2007 Forward and reverse product decompositions of depolarizing Mueller matrices *Opt. Lett.* **32** 689–91

[100] Wood M F, Guo X and Vitkin I A 2007 Polarized light propagation in multiply scattering media exhibiting both linear birefringence and optical activity: monte Carlo model and experimental methodology *J. Biomed. Opt.* **12** 014029

[101] Pierangelo A *et al* 2013 Polarimetric imaging of uterine cervix: a case study *Opt. Express* **21** 14120–30

[102] Rehbinder J, Haddad H, Deby S, Teig B, Nazac A, Novikova T, Pierangelo A and Moreau F 2016 Ex vivo Mueller polarimetric imaging of the uterine cervix: a first statistical evaluation *J. Biomed. Opt.* **21** 71113

[103] Pierangelo A, Benali A, Antonelli M R, Novikova T, Validire P, Gayet B and De Martino A 2011 Ex-vivo characterization of human colon cancer by Mueller polarimetric imaging *Opt. Express* **19** 1582–93

[104] Shukla P and Pradhan A 1600-1609 Mueller decomposition images for cervical tissue: potential for discriminating normal and dysplastic states *Opt. Express* **17** 2009

[105] Chue-Sang J, Bai Y, Stoff S, Straton D, Ramaswamy S and Ramella-Roman J C 2016 Use of combined polarization-sensitive optical coherence tomography and Mueller matrix imaging for the polarimetric characterization of excised biological tissue *J. Biomed. Opt.* **21** 71109

[106] Alali S, Aitken K J, Schroder A, Gribble A, Bagli D J and Vitkin I A 2014 Assessment of local structural disorders of the bladder wall in partial bladder outlet obstruction using polarized light imaging *Biomed. Opt. Express* **5** 621–9

[107] Wood M F, Ghosh N, Wallenburg M A, Li S H, Weisel R D, Wilson B C, Li R K and Vitkin I A 2010 Polarization birefringence measurements for characterizing the myocardium, including healthy, infarcted, and stem-cell-regenerated tissues *J. Biomed. Opt.* **15** 047009

[108] Ahmad M, Alali S, Kim A, Wood M F, Ikram M and Vitkin I A 2011 Do different turbid media with matched bulk optical properties also exhibit similar polarization properties? *Biomed. Opt. Express* **2** 3248–58

[109] Alali S, Ahmad M, Kim A, Vurgun N, Wood M F and Vitkin I A 2012 Quantitative correlation between light depolarization and transport albedo of various porcine tissues *J. Biomed. Opt.* **17** 045004

[110] Wood M F, Cote D and Vitkin I A 2008 Combined optical intensity and polarization methodology for analyte concentration determination in simulated optically clear and turbid biological media *J. Biomed. Opt.* **13** 044037

[111] Wood M F, Ghosh N, Moriyama E H, Wilson B C and Vitkin I A 2009 Proof-of-principle demonstration of a Mueller matrix decomposition method for polarized light tissue characterization in vivo *J. Biomed. Opt.* **14** 014029

[112] Okoro C and Toussaint K C Jr. 2016 Experimental demonstration of two-photon Mueller matrix second-harmonic generation microscopy *J. Biomed. Opt.* **21** 16011

[113] Okoro C and Toussaint K C 2017 Second-harmonic patterned polarization-analyzed reflection confocal microscope *J. Biomed. Opt.* **22** 1–8

[114] de Boer J F and Milner T E 2002 Review of polarization sensitive optical coherence tomography and Stokes vector determination *J. Biomed. Opt.* **7** 359–71

[115] Wojtkowski M 2010 High-speed optical coherence tomography: basics and applications *Appl. Opt.* **49** D30-61
[116] Lurie KL, Moritz T J and Ellerbee AK. 2012 Design considerations for polarization-sensitive optical coherence tomography with a single input polarization state. *Biomed. Opt. Express* **7-8** 2273–87
[117] Fujimoto J G 2002 Optical coherence tomography: technology and applications: *2002 IEEE/LEOS Int. Conf. on Optical Mems, Conf. Digest* 147–8
[118] Hee M R, Huang D, Swanson E A and Fujimoto J G 1992 Polarization-sensitive low-coherence reflectometer for birefringence characterization and ranging *J. Opt. Soc. Am.* B **9** 903–8
[119] de Boer J F, Milner T E, van Gemert M J and Nelson J S 1997 Two-dimensional birefringence imaging in biological tissue by polarization-sensitive optical coherence tomography *Opt. Lett.* **22** 934–6
[120] Cense B *et al* 2005 Spectral-domain polarization-sensitive optical coherence tomography at 850 nm *Proc. SPIE* **5690** 159–62
[121] Yamanari M, Makita S and Yasuno Y 2008 Polarization-sensitive swept-source optical coherence tomography with continuous source polarization modulation *Opt. Express* **16** 5892–906
[122] Baumann B, Augustin M, Lichtenegger A, Harper D, Muck M, Eugui P, Wartak A, Pircher M and Hitzenberger C 2018 Polarization-sensitive optical coherence tomography imaging of the anterior mouse eye *J. Biomed. Opt.* **23** 1–12
[123] Duan L, Makita S, Yamanari M, Lim Y and Yasuno Y 2011 Monte-Carlo-based phase retardation estimator for polarization sensitive optical coherence tomography *Opt. Express* **19** 16330–45
[124] Jiao S, Yu W, Stoica G and Wang L V 2003 Contrast mechanisms in polarization-sensitive Mueller-matrix optical coherence tomography and application in burn imaging *Appl. Opt.* **42** 5191–7
[125] Jiao S L and Wang L H V 2002 Two-dimensional depth-resolved Mueller matrix of biological tissue measured with double-beam polarization-sensitive optical coherence tomography *Opt. Lett.* **27** 101–3
[126] Ding Z Y, Liang C P and Chen Y 2015 Technology developments and biomedical applications of polarization-sensitive optical coherence tomography *Front. Optoelectron* **8** 128–40
[127] Lurie K L, Moritz T J and Ellerbee A K 2012 Design considerations for polarization-sensitive optical coherence tomography with a single input polarization state *Biomed. Opt. Express* **3** 2273–87
[128] Fukuda S, Yamanari M, Lim Y, Hoshi S, Beheregaray S, Oshika T and Yasuno Y 2013 Keratoconus diagnosis using anterior segment polarization-sensitive optical coherence tomography *Investigative Ophthalmol. Vis. Sci.* **54** 1384–91
[129] Fukuda S, Kishino G, Hoshi S, Beheregaray S, Ueno Y, Fukuda M, Kasaragod D, Yasuno Y and Oshika T 2015 Repeatability of corneal phase retardation measurements by polarization-sensitive optical coherence tomography *Invest. Ophthalmol. Vis. Sci.* **56** 3196–201
[130] Gotzinger E, Pircher M, Dejaco-Ruhswurm I, Kaminski S, Skorpik C and Hitzenberger C K 2007 Imaging ofbirefringent properties of keratoconus corneas by polarization-sensitive optical coherence tomography *Invest. Ophthalmol. Vis. Sci.* **48** 3551–8
[131] Baumann B *et al* 1670-1683 Polarization sensitive optical coherence tomography of melanin provides intrinsic contrast based on depolarization *Biomed. Opt. Express* **3** 2012
[132] Zotter S *et al* 2013 Measuring retinal nerve fiber layer birefringence, retardation, and thickness using wide-field, high-speed polarization sensitive spectral domain OCT *Investigative Ophthalmol. Vis. Sci.* **54** 72–84
[133] Schutze C, Teleky K, Baumann B, Pircher M, Gotzinger E, Hitzenberger C K and Schmidt-Erfurth U 2016 Polarisation-sensitive OCT is useful for evaluating retinal pigment epithelial lesions in patients with neovascular AMD *Br. J. Ophthalmol.* **100** 371–7
[134] Gotzinger E, Pircher M, Geitzenauer W, Ahlers C, Baumann B, Michels S, Schmidt-Erfurth U and Hitzenberger C K 2008 Retinal pigment epithelium segmentation by polarization sensitive optical coherence tomography *Opt. Express* **16** 16410–22
[135] Wang Y, Zhang K, Duan D and Yao G 2017 Heart structural remodeling in a mouse model of Duchenne cardiomyopathy revealed using optical polarization tractography *Biomed. Opt. Express* **8** 1271–6
[136] Dhadwal G, Ortiz-Policarpio B, McLean D, Diao D, Lui H, Tchvialeva L and Lee T 2013 In vivo laser speckle measurement of skin roughness versus profilometric measurement of silicone replicas *J. Am. Acad. Dermatol.* **68** Ab36-Ab36
[137] Doronin A, Tchvialeva L, Markhvida I, Lee T K and Meglinski I 2016 Backscattering of linearly polarized light from turbid tissue-like scattering medium with rough surface *J. Biomed. Opt.* **21** 071117
[138] Ramella-Roman J, Prahl S and Jacques S 2005 Three Monte Carlo programs of polarized light transport into scattering media: part I *Opt. Express* **13** 4420–38